# Fabrication and Characterization of Aluminum SQUID Transmission Lines

Luca Planat, Ekaterina Al-Tavil, Javier Puertas Martínez, Rémy Dassonneville, Farshad Foroughi, Sébastien Léger, Karthik Bharadwaj, Jovian Delaforce, Vladimir Milchakov, Cécile Naud, et al.

# Fabrication and Characterization of Aluminum SQUID Transmission Lines

Luca Planat, Ekaterina Al-Tavil, Javier Puertas Martínez, Rémy Dassonneville, Farshad Foroughi, Sébastien Léger, Karthik Bharadwaj, Jovian Delaforce, Vladimir Milchakov, Cécile Naud, Olivier Buisson, Wiebke Hasch-Guichard, and Nicolas Roch*

*Université Grenoble Alpes, CNRS, Grenoble INP, Institut Néel, 38000 Grenoble, France*

(Received 23 July 2019; revised manuscript received 6 October 2019; published 6 December 2019)

We report on the fabrication and characterization of flux-tunable, low-loss, superconducting-quantum-interference-device- (SQUID) based transmission lines whose impedance is close to 50 Ω. The fabrication process relies on the deposition of a thin dielectric layer (few tens of nanometers) by atomic layer deposition on top of a SQUID array. The whole structure is covered by a nonsuperconducting metallic top-ground plane. We present experimental results from five different samples. We systematically characterize their microscopic parameters by measuring the propagating phase in these structures. We also investigate losses and discriminate conductor losses from dielectric losses. This fabrication method offers several advantages. First, the SQUID-array fabrication relies not on a niobium-trilayer process but on a simpler, double-angle evaporation technique. Second, atomic layer deposition provides a high-quality dielectric, leading to low-loss devices. Furthermore, the SQUID-array fabrication is based on a standard, all-aluminum process, allowing direct integration with superconducting qubits. Moreover, our devices are *in situ* flux tunable, allowing mitigation of uncertainty inherent in any fabrication process. Finally, because the unit cell is a single SQUID (no extra ground capacitance is needed), it is straightforward to modulate the size of the unit cell periodically, allowing band engineering. This fabrication process can be directly applied to traveling-wave parametric amplifiers.

DOI: 10.1103/PhysRevApplied.12.064017

## I. INTRODUCTION

Being able to reproduce the rich physics of nonlinear fiber optics [1] in the microwave domain would be a major milestone in microwave physics, since the nonlinearities that occur in this frequency range are orders of magnitude larger than in the optical domain. Nonlinear optical fibers have resulted in fiber amplifiers, a key technology for communication systems, but are also very appealing in quantum optics since their dispersion can be tailored to create photonic crystals, allowing the investigation of phenomena such as frequency translation of single photons [2]. In the microwave domain, electrical signals propagate in transmission lines [3]. The quantum nature of these microwave photons can usually be disregarded, unless the circuits in which they propagate are cooled to very low temperatures (below 100 mK). Under these conditions, we speak about circuit quantum electrodynamics [4]. While in the optical domain nonlinearity can be enhanced by doping fibers with rare-earth materials, microwave superconducting quantum circuits can be made strongly nonlinear and low loss by combining superconducting materials and Josephson junctions [5] or by taking advantage of the self-nonlinearity of disordered superconductors [6]. This approach has been very successful and led to the observation of strong light-matter coupling [7], resonance fluorescence with extinction as high as 94% [8], and near-quantum-limited parametric amplifiers [9] since it combines both dissipationless and very nonlinear characteristics. However, all these experiments rely on resonant structures—the microwave equivalent of optical cavities.

So far, only few experiments have used nonlinear transmission lines—-the microwave equivalent of nonlinear optical fibers—in the quantum regime. One notable exception is the demonstration of traveling-wave parametric amplifiers based on either Josephson junctions [10,11] or disordered superconductors [12–15]. The small number of experimental implementations is explained by the fact that fabricating a long, low-loss, impedance-matched, nonlinear transmission line is very demanding. In the case of a Josephson-junction transmission line, nonlinearity is strong [16], sparing the need for long structures. The challenge here is to lower the naturally large impedance of Josephson-junction arrays [17] compared to 50 Ω—by increasing their capacitive effect to the ground, which requires very concentrated capacitors—while maintaining sufficiently low losses. Combining all these

*nicolas.roch@neel.cnrs.fr

 

requirements was demonstrated with a complex niobium-trilayer fabrication process [18]. Disordered superconductor transmission lines, on the other hand, are mainly limited by their relatively weak nonlinearity. Obtaining sizable nonlinear quantum effects requires meter-long structures, which are strongly prone to fabrication defects [13,19].

In this work, we present a superconducting-quantum-interference-device- (SQUID) based transmission line (STL) fabricated by a simple, aluminum-based process. Impedance matching is obtained via a top-ground plane separated from the SQUID array by a very thin alumina layer. Such STLs show losses on par with previously reported values [10] and a characteristic impedance close to 50 Ω. This impedance can be adjusted *in situ*, owing to the flux tunability of the structure [20]. Furthermore, because of the simple architecture of our STL, the impedance of each unit cell can be tailored at will to create photonic-crystal-like transmission lines [21,22]. In this article two types of devices, based on the exact same fabrication process, are presented: a 50-Ω-matched STL and resonant structures made of a shorter STL. The latter are used as test structures to characterize our fabrication process in the single-microwave-photon regime.

This article is organized as follows. In Sec. II we introduce the fabrication flow and the microwave design of the STL. Section III presents the low-temperature microwave properties of five different devices. Sections IV and V focus on the microscopic origins of STL losses and their strong power dependence, respectively. In Sec. VI, the magnetic flux response of the STL is presented.

## II. FABRICATION PROCESS

In this section we detail the fabrication process for SQUID-based transmission lines. Four different batches are obtained by this process. Five different devices are then characterized at very low temperatures, as reported in Table I. The devices are fabricated on high-resistivity silicon substrates (thickness 275 $\mu$m).

The back side of the silicon wafer is covered by a thin layer of titanium (10 nm, for adhesive purposes) and a thick layer of gold (200 nm) to ensure good thermal and electrical contact with the sample holder. The fabrication process relies on three simple steps as summarized in Fig. 1. First a SQUID array is fabricated by double-angle evaporation of aluminum (MEB550S evaporator from Plassys), separated by an *in situ* oxidation to grow the tunnel barrier. For batches 1, 2 and 3, the oxidation pressure is 4 Torr, and for batch 4, it is 1 Torr. The resist mask is patterned with a 100-keV electron-beam writer (model nB5 from NanoBeam) to allow bridge-free fabrication [23]. The typical size of a single Josephson junction is 10 $\mu$m high and 0.5 $\mu$m wide (see Appendix A). A unit cell (two Josephson junctions plus connecting wires in a loop) is about 3 $\mu$m wide. This technique allows fabrication of low- disorder arrays combining up to 2000 unit cells [24]. However, one of the main difficulties in fabricating such long arrays is stitching errors, arising from a wrong focus of the electron beam due to unavoidable tilt of the substrate. To overcome this, we use the *focus-map* feature of our electron-beam writer, allowing us to readjust dynamically the focus during the writing process. This is achieved by fitting, before the writing process, the surface of the chip ($8.1 \times 8.1$ mm$^2$) by a tilted plane. The fit

TABLE I. Summary of the five samples presented in this article. Four are transmission lines (TLs) and one is a resonator (Res). The main fabrication characteristics, SQUID characteristics, and loss coefficients are summarized. The values of flux-dependent parameters are reported at zero flux bias. Calibration methods are also reported.

| Device | A | B | C | D | E |
|---|---|---|---|---|---|
| Batch | 1 | 2 | 2 | 3 | 4 |
| Type | TL | TL | Res | TL | TL |
| Oxidation pressure (Torr) | 4 | 4 | 4 | 4 | 1 |
| ALD temperature (°C) | 150 | 150 | 150 | 200 | 150 |
| Dielectric thickness (nm) | 38 | 38 | 38 | 28 | 28 |
| Ground thickness (nm) | 200 | 400 | 400 | 400 | 1000 |
| Ground material | Au | Au | Au | Au | Cu |
| Josephson-junction size, $H$ ($\mu$m) $\times$ $W$ ($\mu$m) | $12.0 \times 0.45$ | $10.5 \times 0.40$ | $10.5 \times 0.40$ | $12.0 \times 0.45$ | $12.0 \times 0.45$ |
| $L_J$ (pH) | 88.1 | 127 | 137 | 140 | 58.7 |
| $C_J$ (fF) | 490 | 380 | 380 | 485 | 485 |
| $C_g$ (fF) | 31 | 25 | 25 | 43 | 43 |
| $Z_c$ (Ω) | 53 | 71 | 74 | 57 | 37 |
| Phase velocity ($10^6$ m s$^{-1}$) | 1.96 | 1.76 | 1.62 | 1.32 | 2.06 |
| $\tan\delta$ ($10^{-3}$) | 6.5 | 6.0 | 5.0 | 4.0 | 6.5 |
| $L_c$ ($10^{-4}$) (m$^{-1}$ Hz$^{-1/2}$) | 2.5 | 1.0 | ... | 0.8 | ¡0.1 |
| Phase-calibration method | Switch | Switch | not applicable | Dummy | Dummy |

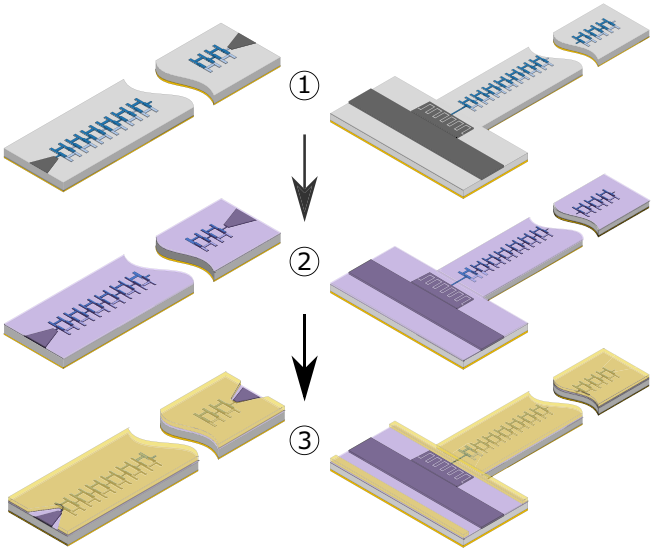


FIG. 1. Fabrication flow for SQUID-based transmission lines and resonators. Step 1, fabrication of long SQUID arrays using electron-beam lithography and double-angle evaporation of aluminum. Step 2, deposition of a conformal alumina layer by ALD. Step 3, evaporation of a thick metallic layer (gold or copper) acting as an electrical ground. This layer is patterned by a combination of electron-beam lithography and lift-off.

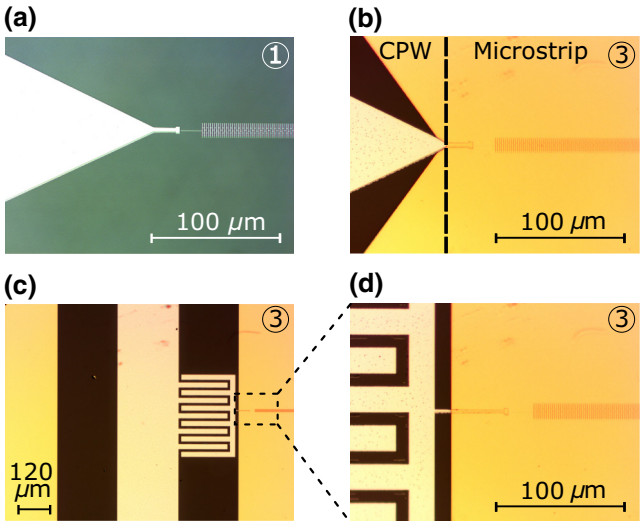


FIG. 2. Samples from the first batch. (a),(b) SQUID-based transmission lines. (c),(d) Resonant structures used as control samples. Every picture is labeled by a number corresponding to the fabrication step as shown in Fig. 1. (a) Input of the SQUID-based transmission line after the first step. The left side shows the bonding pad with a tapered shape, and the right side shows a few dozen SQUIDs. (b) Same structure but after step 3. The gold layer is deposited everywhere but on the bonding pad. SQUIDs are still distinguishable from below the alumina and gold layers. (c) The resonant structure after step 3. The feedline is visible in the middle. On the right side an interdigitated capacitor coupling the feedline to a section of the SQUID-based transmission line (623 unit cells) is shown. (d) Enlargement.

is done by our measuring the height of the four corners where gold marks were previously deposited. The array is terminated by tapered bonding pads (coupling capacitance) as shown in Fig. 2(b) [Fig. 2(d)]. During step 2, a thin film of alumina is deposited by atomic layer deposition (ALD) with a Savannah system from Cambridge Nanotech. The sample is inserted inside a chamber pumped down to 0.29 mbar. We try two different deposition temperatures, 150 and 200 °C, to infer the effect of temperature on the dielectric quality. These temperatures correspond to the chamber of the ALD system, where the wafer stays during deposition. Thicknesses of the various films are reported in Table I. ALD films combine low microwave losses and conformal deposition. This latter property is crucial to guarantee electrical isolation between the SQUID and the top-ground plane deposited during step 3. Access to the bonding pads is guaranteed by windows in this metallic layer. These openings are obtained by a second lithography step and lift-off of the metallic film. We check that the thickness of the alumina layer is not affected by this subsequent step. Finally, we can easily contact the bonding pads through the alumina layer using microbonding given the thickness of this layer (less than 40 nm). Regarding microwave engineering, we design the SQUID arrays as a 50-Ω microstrip transmission line. Since our SQUIDs display a typical inductance $L \approx 100$ pH and a characteristic impedance $Z_c = \sqrt{L/C_g} \approx 50\ \Omega$ is being sought, it requires a shunt capacitance $C_g \approx 40$ fF.

We model $C_g$ as a planar capacitance $C_g = \epsilon_0 \epsilon_r S/t$ (where $\epsilon_0$ is the vacuum permittivity and $S$ is the SQUID's area). Given we are using alumina as the insulator (dielectric constant $\epsilon_r \approx 9.8$), this translates into a dielectric thickness $t \approx 30$ nm. These numbers lead to a transmission line with a microstrip geometry with unique features, such as wave velocity below 1% of the light velocity while being matched to a 50-Ω environment. We also design a smooth transition from a microstrip geometry to a coplanar-waveguide (CPW) geometry to allow for large bonding pads. This transition is shown in Fig. 2(b). We use a conventional tapered shape to keep the impedance constant between the bonding pad and the CPW-microstrip transition. Strictly speaking, this is not a CPW geometry since the aluminum layer and the top ground are not exactly in the same plane as they are separated by the alumina layer. Nevertheless, electromagnetic simulations show that the electric field profile is not altered, and that approximating this geometry as a CPW is correct. Indeed alumina and silicon have similar dielectric constants, and a step of a few tenths of a nanometer is negligible compared with the lateral distance between the aluminum and the ground of a few-hundred micrometers. Regarding

resonators, the section of the SQUID-based transmission line (length approximately 600 unit cells) is capacitively coupled to a feedline as shown in Figs. 1, 2(c), and 2(d).

## III. CRYOGENIC MICROWAVE PROPERTIES

We now turn to the microwave characterization of these samples at very low temperature ($T = 25$ mK). Measurements are performed with a standard cryogenic setup. First we measure the dispersion relation (angular frequency versus wave vector) of the samples. The experimental protocol to access such quantities is not the same for the transmission lines and the resonant structures. For the latter, two-tone spectroscopy is used [25,26], whereas for the former, procedure explained in Ref. [10] is followed. The idea is to measure the propagating phase $\phi$ of a microwave tone along the device under test (DUT). A proper calibration is needed to remove the contribution of the cryogenic measurement setup. To do so, we use two calibration techniques. For samples A and B, a cryogenic microwave switch (model R577433000 from Radiall) shunts the sample at $T = 25$ mK to infer, during the same cooldown, the contribution of both the setup and the DUT. To calibrate the contribution of the setup for samples D and E we use a dummy instead of the actual chip containing the SQUID-based transmission line. This technique requires two different cooldowns but gives a better estimate of the setup contribution (wire bonds are similar to the DUT and there are no extra cables connecting the switch to the DUT).

The last calibration step is to ensure that at zero frequency this propagating phase is zero. Indeed the phase measured with a vector network analyzer is defined modulo $2\pi$. We use a procedure similar to Macklin *et al.* [10] to adjust it properly. The propagating phase $\phi$ can then be linked to the wave vector $k$ by

$$k(\omega) = \frac{\phi(\omega)}{L}, \tag{1}$$

where $L$ is the length of the SQUID array and is perfectly known since both the unit cell size $a$ and the total number of unit cells $N_J$ are well known. Two measured dispersion relations are plotted in Fig. 3. Gray points in Fig. 3(a) were discarded from the fitting procedure since they are out of the operating-frequency range (3–14 GHz) of our cryogenic HEMT amplifier (model LNF-LNC1-12A from Low Noise Factory).

To infer the microscopic parameter of the samples $L_J$ (see Appendix A), we fit their dispersion relations using the following model [26]:

$$\omega_k = \omega_{\text{plasma}} \sqrt{\frac{1 - \cos ka}{1 - \cos ka + C_g/2C_J}}, \tag{2}$$

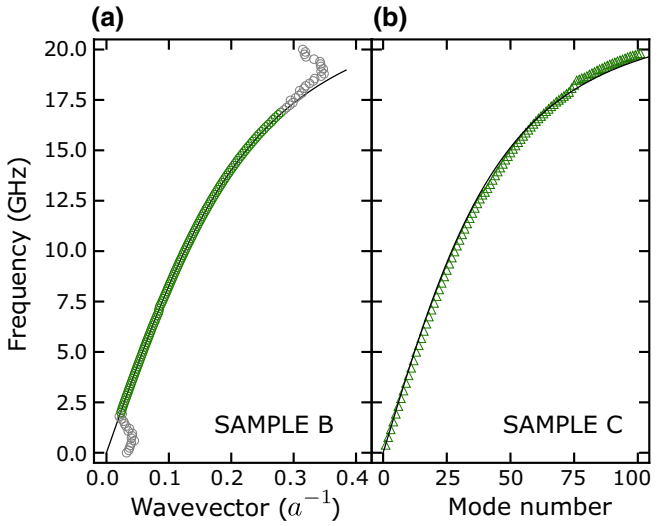


FIG. 3. Dispersion relations. (a) Dispersion relation of a SQUID-based transmission line (sample B). The black line is a fit of the experimental data to Eq. (2). (b) Dispersion relation of a resonant structure (sample C). Data are acquired by two-tone spectroscopy and fitted with Eq. (2) as well.

where the Josephson capacitance $C_J$ and $C_g$ are fixed parameters. $C_J$ is taken as 45 fF/$\mu$m$^2$ [27]. As said, $C_g$ is modeled and calculated as a parallel-plate capacitor given that the geometrical parameters and dielectric constant are known. $\omega_{\text{plasma}}$ is the plasma frequency of a SQUID and reads $\omega_{\text{plasma}} = 1/\sqrt{L_J C_J}$. For $L_J$, we experience a drift from batch 1 to batch 3 toward larger inductance. Junctions from batch 4 are oxidized with a pressure of 1 Torr instead of 4 Torr to compensate for this drift. Also, samples B and C should display the same microscopic parameters since they are fabricated in the same batch (see Table I). The size of sample-B unit cells is modulated periodically, while sample C has uniform cells. This modulation is very small (6% amplitude) and only opens a small photonic gap over a band of a few-hundred megahertz in the dispersion relation. This does not affect its overall shape, as shown in Fig. 2, where only a small kink can be seen around 7 GHz. We find a difference below 10% between the two fitted $L_J$ values, which might come from the fitting procedure or inhomogeneity in the oxidation of junctions over the 2-in. wafer. Finally, we can define a low-frequency ($\omega \ll \omega_{\text{plasma}}$) characteristic impedance $Z_c = \sqrt{L_J/C_g}$ for both samples, leading to $Z_c$ between 71 and 74 Ω at zero flux bias. $L_J$ is power dependent, and we observe an increase of a few picohenries when the microwave current is close to the SQUID critical current. This effect is at the heart of parametric amplification in such nonlinear transmission lines [10] as we reported in Ref. [22].

## IV. CONDUCTOR AND DIELECTRIC LOSSES

Losses of the transmission line are another very important parameter. To understand the loss mechanisms

we probed the calibrated transmission of the STL using the calibration technique described in the previous section. Figure 4 shows this calibrated transmissions for samples A, B, D, and E. They show losses on the order of 5 dB/cm at 6 GHz. Although these losses are significant, they are comparable to those of previously reported structure based on Josephson junctions[10]. A more-thorough study can explain the different loss mechanisms of our devices. Seen as microstrip lines, our samples suffer from two well-known phenomena in microwave engineering: dielectric and conductor losses [28]. Within the superconducting community, the latter form of losses have been rightfully ignored since there are no significant losses inside superconductors or in thick metallic grounds (superconducting or not). Such assumptions are not valid anymore in our geometry. Although the central conductor is superconducting, the top-ground plane is made of a nonsuperconducting metal (gold or copper, for the last version), with a finite thickness (hundreds of nanometers), comparable to the skin depth. This configuration can lead to non-negligible conductor losses, as we see later. To determine the origin of the losses, we fit the calibrated transmission of the STL with a simple model [3], where $\alpha_c$ and $\alpha_d$ represent the conductor and dielectric losses, respectively. The total attenuation of the line can then be expressed as

$$A = e^{(\alpha_c+\alpha_d)L}. \tag{3}$$

Considering our microstrip geometry with very large shunt capacitance, it is safe to assume that the electrical field is mainly confined within the top alumina substrate.

Thus, we model the dielectric loss $\alpha_d$ as [3]

$$\alpha_d = \frac{k\tan\delta}{2}. \tag{4}$$

We thus have a direct relation between the angular frequency $\omega_k$ of the signal and the dielectric loss through a free parameter, $\tan\delta$. In microwave engineering, it is defined as the ratio of the imaginary part to the real part of the complex permittivity of the medium. Regarding $\alpha_c$, as mentioned before, we take into account only the top-ground loss. Given the microstrip geometry of the STL where $W$, the width of the transmission line, is much bigger than the dielectric thickness $t$, fringing fields can be ignored [29] and conductor losses can be modeled as [3,29]

$$\alpha_c = \frac{R_s}{Z_c W}, \tag{5}$$

where $Z_c$ is the characteristic impedance of the line and $R_s$ is the *surface resistivity* of the conductor. In a normal conductor, surface resistivity is related to its skin depth $\delta_s = \sqrt{2/\omega\mu_0\sigma}$. On the one hand, if a conductor is much thicker than its skin depth, the surface resistivity is independent of its thickness and is taken as $R_{s,0} = \sqrt{\omega\mu_0/2\sigma}$, where $\mu_0$ is the vacuum permeability and $\sigma$ is the conductor conductivity.

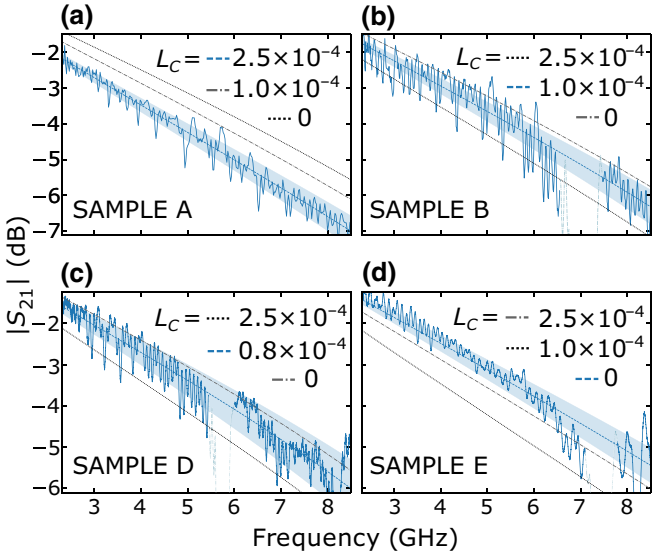


FIG. 4. Calibrated, low-temperature transmission of the STL. Solid lines are experimental data and dashed lines are fits to Eq. (3). Values of the fitting parameters are reported in Table I. Shaded blue areas represent $5 \times 10^{-4}$ uncertainty on $\tan\delta$. Dotted black and dash-dotted gray lines are obtained with Eq. (3) with the same $\tan\delta$ but with different conductor loss (values indicated in each panel are in the unit of per meter per square root of hertz). All data are taken with input power $P_{\text{in}} = -106 \pm 3$ dBm except for sample A, where $P_{\text{in}} = -101 \pm 3$ dBm.

On the other hand, if the conductor thickness is comparable to or smaller than the skin depth, alternating current flows through a narrower area, which increases the effective surface resistivity compared with $R_{s,0}$ [29], and thus increases conductor losses as modeled in Eq. (5). Obtaining a value for the surface resistivity in that case would require a detailed three-dimensional electromagnetic simulation and is beyond the scope of this paper. However, the surface resistivity can be seen as a free parameter, and conductor loss can be modeled as

$$\alpha_c = L_c\sqrt{f} \tag{6}$$

under the assumption that $R_s$ remains proportional to $\sqrt{f}$, where $f$ is the signal frequency and $L_c$ is a prefactor accounting for the conductor loss, which should decrease when the thickness of the top-ground metal increases. Then we fit the attenuation of the various STLs characterized in this work using two parameters: $\tan\delta$ and $L_c$. Although STL attenuation shows a monotonous trend versus frequency (see Fig. 4), we manage to fit independently these two parameters. Indeed surface resistivity depends on the square root of the signal frequency, and dielectric loss varies linearly with frequency. In other words,

dielectric loss sets the slope of the insertion loss at high frequencies, while conductor loss affects the lower frequencies. All the fitting parameters obtained are presented in Table I. We now turn to the discussion of these parameters. First we find that $\tan\delta$ remains between $6.5 \times 10^{-3} \pm 5 \times 10^{-4}$ and $4 \times 10^{-3} \pm 5 \times 10^{-4}$ for low-power measurements, which is on par with a previously demonstrated Josephson-junction transmission line [10]. Table I summarizes the different deposition parameters for alumina. We observe that a higher deposition temperature seems to lowers dielectric loss. However, given the uncertainty in the loss tangent in this study, we do not claim that the deposition temperature is the most-important parameter to reduce dielectric loss. However, such values of the loss tangent are very promising, since they are already comparable to the state of the art. Moreover, loss tangents as low as $2.45 \times 10^{-3}$, in the single-photon regime, were reported for alumina with similar thickness at very low temperatures [30]. Regarding conductor loss, we observe that as the top-ground thickness increases, $L_c$ drops. We plot what we consider to be the best conductor loss (in dashed blue lines) for each version as well as other values of conductor loss (in dashed gray lines) to give insight into the confidence interval (see Fig. 4). As a reminder, batches 2 and 3 should have the same conductor loss since their top-ground thickness is the same. Another interesting point is that the conductivity of gold sheets for different thickness $t_s$ has been measured at very low temperatures [31]. The authors of that work reported conductivity of 0.9 GS/m ($t_s = 183$ nm) and 2.5 GS/m ($t_s = 877$ nm). At 7 GHz, the corresponding skin depths $\delta_s$ are 200 and 120 nm, respectively. Batch 1, where the top-ground thickness is similar to the skin depth, shows strong conductor loss. In the other batches, with thicker ground planes, losses decreased until batch 4 (thickness 1 $\mu$m), where the conductor loss is below our experimental resolution and is consistent with the previously reported gold conductivity [32].

## V. POWER-DEPENDENT LOSSES

We now report the power dependence of these losses. In both the matched transmission lines and the resonant structures we observe that losses decrease when power increases (Fig. 5). The fitted loss tangent of the STL presented in Fig. 5(a) depends on the input power and saturates at low power, close to $\tan\delta = 7.5 \times 10^{-3} \pm 5 \times 10^{-4}$. Fitted external and internal quality factors of a given resonant mode are plotted in Fig. 5(b) for various input powers in the feedline. The external quality factor remains constant, while the internal quality factor increases with input power. This observation is in agreement with what was reported in a Josephson-junction transmission line [10]. At very low powers, close to the single-photon regime, losses saturate. This is consistent

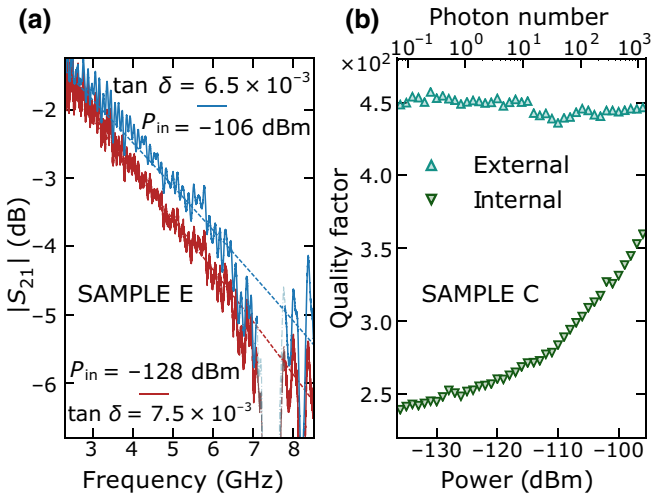


FIG. 5. Power dependence of losses. For both panels, power is referred to the input of the device. (a) STL calibrated transmission (sample E). Input power and fitted loss tangent are reported directly on the figure. (b) Quality factors (internal and external) of a given resonant mode of sample C (angular frequency $\omega_0 = 2\pi \times 7.47$ GHz). Fit is obtained for the same resonance at various input powers (see Appendix B). Photon number (top axis) is obtained using Eq. (B2).

with the presence of two-level systems within the dielectric layer [30]. The internal quality factor and loss tangent are linked by $Q_i = 1/\tan\delta$ [3]. We can compare quality factors from sample C, which is from the same batch as sample B [calibrated transmission is shown in Fig. 4(b)]. For sample B, at low signal power, close to the loss-tangent saturation, we find $\tan\delta = 6.0 \times 10^{-3} \pm 5 \times 10^{-4}$. We compare this value with low-power quality factors measured for sample C. At $P_{\rm in} = -136$ dBm [33] ($\bar{n} \approx 0.1$) we find, depending on the resonant mode, an internal quality factor between $Q_{i,\rm min} = 125$ and $Q_{i,\rm max} = 300$, with a mean value around 200 (see Appendix C). This translates into a loss tangent of $\tan\delta_{\rm mean} = 1/200 = 5.0 \times 10^{-3}$, in good agreement with the loss tangent found for sample B.

## VI. FLUX MODULATION

Finally, we describe the flux tunability of a STL. Figure 6(a) shows the flux dependence of the transmission of sample A. At low frequencies, below 8 GHz, the transmission is mostly flat with no visible ripples. At higher frequencies one can observe flux-dependent standing waves. This is explained by spurious reflections between the STL and its microwave environment. These reflections could be caused by wire bonds or a nonoptimized printed-circuit-board-to-connector transition. We emphasize the smooth behavior of the device during flux tuning, despite the large number of SQUIDs. This stability can be attributed to our choice of having a nonsuperconducting ground plane on top of the SQUID, which prevents flux trapping and effects

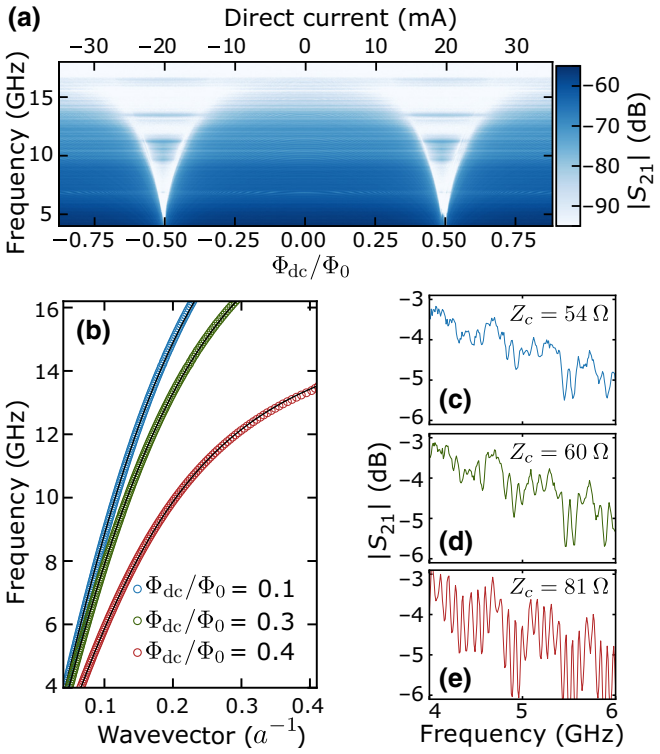


FIG. 6. Flux dependence of sample-A transmission. (a) Raw transmission as a function of flux and frequency. (b) Experimental dispersion relation and fits taken at three different magnetic fluxes. (c)–(e) Calibrated transmission. The colors correspond to the same color coding as in (b). The characteristic impedances displayed in the top-right corners are extracted from the fits in (b).

due to Meissner currents. The plasma frequency of the SQUID can be directly observed as a drop in transmission. At zero flux it is above 20 GHz but drops almost to zero for magnetic fluxes close to half a fluxoid. We show dispersion relations for sample A taken at three different magnetic fluxes in Fig. 6(b). As expected, the magnetic flux affects the general shape of the dispersion (linear part and the plasma frequency). Fitting these dispersion relations with Eq. (2) allows us to extract the characteristic impedance $Z_c$ at different magnetic fluxes. In Figs. 6(c)–6(e) we show an enlargement of the calibrated transmission over a small frequency window. Figs. 6(c)–6(e) use the same scales for the $x$ axis and the $y$ axis. The characteristic impedance is extracted from the fits shown in Fig. 6(b). As $Z_c$ moves away from 50 Ω, the wiggle amplitude increases.

## VII. CONCLUSION

We introduce a process to fabricate SQUID-based transmission lines. It is simple, is low loss, and offers *in situ* flux tunability. The impedance matching to 50 Ω relies on a simple yet effective idea: a metallic electrical ground deposited on top of the SQUID array, which are separated by a thin alumina layer, guaranteeing electrical isolation. Impedance matching is demonstrated at very low temperatures (20 mK) and very low power (single-photon regime). Two loss sources are identified; conductor losses due to the finite thickness of the metallic ground compared with the skin depth and dielectric losses consistent with the presence of two-level systems. We show that increasing the thickness of the ground plane decreases conductor losses. Regarding dielectric losses, we measure the loss tangent down to $5.0 \times 10^{-3}$. This value is comparable to what was reported in the literature [10] but could be decreased given the values previously obtained for alumina [30]. Finally, we demonstrate *in situ* flux tunability of these STLs. These devices could be used as Josephson traveling-wave parametric amplifiers, based on four-wave mixing [10,11,22]. Their flux tunability offers interesting perspectives regarding three-wave mixing [34,35] or Kerr-free [36,37] Josephson traveling-wave parametric amplifiers. These devices could also be used to perform new quantum-optics experiments in the microwave domain [38].

## ACKNOWLEDGMENTS

Very fruitful discussions with D. Basko, K.R. Amin, and A. Ranadive are acknowledged. We also thank M. Selvanayagam for critical reading of the manuscript, L. Cagnon for his help with the atomic layer deposition, P. David for help with the fabrication of the top ground and T. Crozes for his assistance with the e-beam writer. The samples were fabricated in the Nanofab clean room. We also thank L. Cagnon for his help with the atomic layer deposition. This research was supported by the ANR under contract CLOUD (project number ANR-16-CE24-0005) and the European Union's Horizon 2020 research and innovation program under Grant Agreement No. 824109, the European Microkelvin Platform. J.P.M. acknowledges support from the Laboratoire d'excellence LANEF in Grenoble (Grant No. ANR-10-LABX-51-01). R.D. and S.L. acknowledge support from the CFM Foundation and the Investisements d'avenir (Grant No. ANR-15-IDEX-02) programs of the French National Research Agency. K.B. and J.D. acknowledge the European Union's Horizon 2020 research and innovation programme under the Marie Sklodowska-Curie Grant Agreement No 754303.

## APPENDIX A: ELECTRICAL MODELS

In this section, we present the electrical models used to describe the samples we measure. For the STL, we use a standard telegrapher model where one SQUID is a cell composed of a nonlinear Josephson inductance $L_J$, a ground capacitance $C_g$, and a Josephson capacitance $C_J$. The electrical sketch is shown in Fig. 7(a). The SQUID array is connected to 50-Ω pads by wire bonding. For the SQUID-based resonator, we use the same model. The only

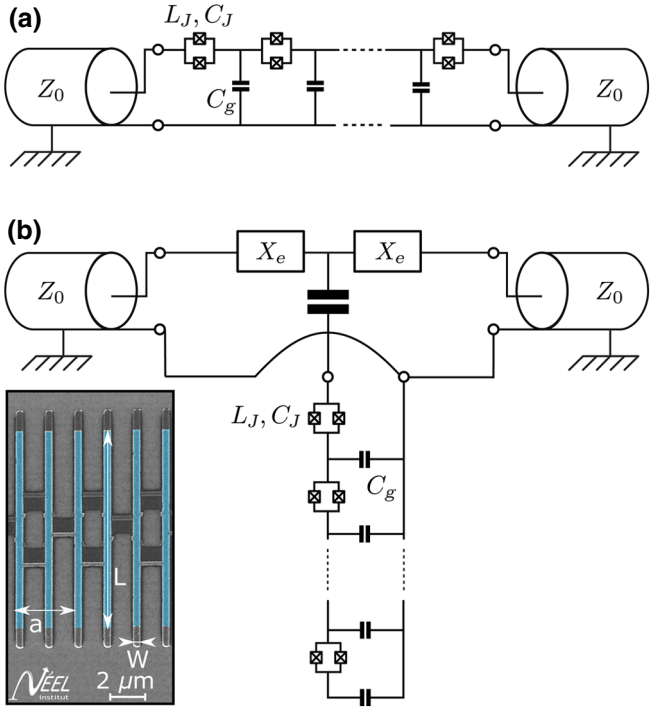


FIG. 7. Electrical sketches of the two measured structures. (a) Electrical model of the STL. (b) Electrical model of the SQUID-based resonator. The inset shows an SEM picture of three SQUIDs. Highlighted blue regions are Josephson junctions.

difference is that the line is capacitively coupled to the 50-Ω feedline. An electrical sketch is shown in Fig. 7(b).

## APPENDIX B: SQUID-BASED-RESONATOR MEASUREMENTS

We present here low-temperature measurements of sample C. It is 600 SQUIDs long with a free spectral range of 350 MHz. Transmission close to resonance is fitted with the formula [39]:

$$S_{21} = \frac{Z_0}{Z_0 + iX_e} \frac{1 + 2iQ_i\left(\dfrac{\omega - \omega_0}{\omega_0}\right)}{1 + \dfrac{Q_i(Z_0 + iX_e)}{(Q_e Z_0)} + 2iQ_i\left(\dfrac{\omega - \omega_0}{\omega_0}\right)}, \tag{B1}$$

where $Z_0$ is the feedline characteristic impedance, $X_e$ is the reactance from the bonding wires, $\omega_0$ the resonance frequency of the resonator, and $Q_i$ and $Q_e$ are the internal and external quality factors, respectively. In Fig. 8 we present five resonances from 6.00 to 7.75 GHz (amplitude and phase) from the SQUID-based resonator at very low input power. The black lines are fits to Eq. (B1). From this equation we extract internal and external quality factors [see Fig. 5(b)], which we plot as a function of input power

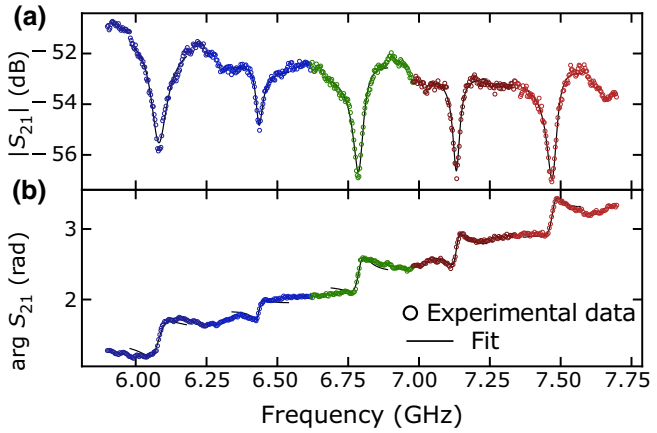


FIG. 8. Transmission $S_{21}$ of the hanger resonators fitted close to the resonances.

and photon number inside the cavity. The photon number is calibrated with use of input-output theory [39]:

$$\bar{n} = \frac{2\dfrac{\omega_0}{Q_e}}{\hbar\omega_0\left(\dfrac{\omega_0}{Q_e} + \dfrac{\omega_0}{Q_i}\right)^2} P_{\text{in}}, \tag{B2}$$

where $\omega_0$ is the resonant frequency of the mode and $P_{\text{in}}$ is the signal input power.

## APPENDIX C: FREQUENCY DEPENDENCE OF INTERNAL QUALITY FACTORS

In this section, we present extracted quality factors for very low input power, $P_{\text{in}} = -136 \pm 3$ dBm, which

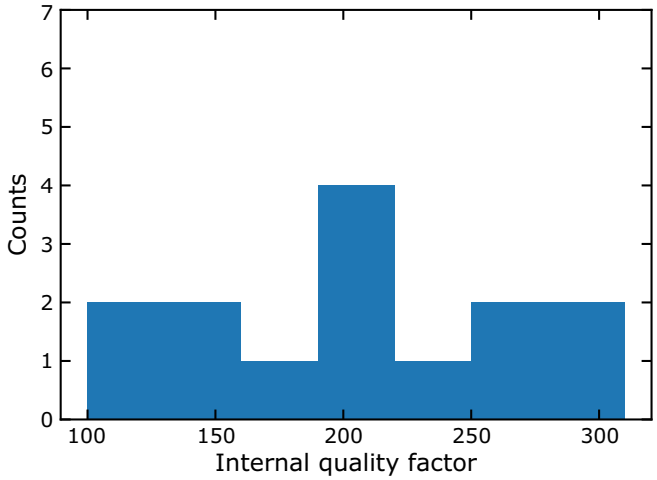


FIG. 9. Internal quality factors extracted from the fit of 14 modes in sample C between 3.8 and 8.46 GHz at input power $P_{\text{in}} = -136 \pm 3$ dBm, corresponding to the single-photon level. We observe a spread of the internal quality factor of around 200 at this power.

translates into 0.1 photon (see Appendix B for the photon-number calibration). At very low photon number, close to the saturation of the losses, we observe an internal quality factor of 200 with a spread between 125 and 300 for different resonant frequencies, as shown in Fig. 9.

## APPENDIX D: EXPERIMENTAL SETUP

In this section, we present the experimental setup in Fig. 10(a) and the two calibration techniques in Fig. 10(b) and 10(c). The microwave setup is a standard circuit-quantum-electrodynamics experimental setup, where the DUT stands on a 25-mK stage. The experimental scattering coefficients are measured with a ZNB20 vector network analyzer from Rhode & Schwartz. To generate the dc magnetic flux $\Phi_{dc}$ threading the SQUID's loops, a superconducting coil is put just above the sample. This coil is biased by a 3245A dc source from Hewlett-Packard. For samples A and B, calibration of the setup is done by our connecting a four-port microwave switch between the samples and the rest of the setup. This allows an in situ calibration since it can be switched while the dilution refrigerator is cold by sending an electrical pulse to the switch. The phase propagation in the cables between the switch and the sample must be canceled by measuring precisely the propagation constant of these cables. For samples D and E, calibration is done by our measuring before the samples a dummy of the sample during a dedicated cooldown. This dummy is a 50-Ω CPW transmission line.

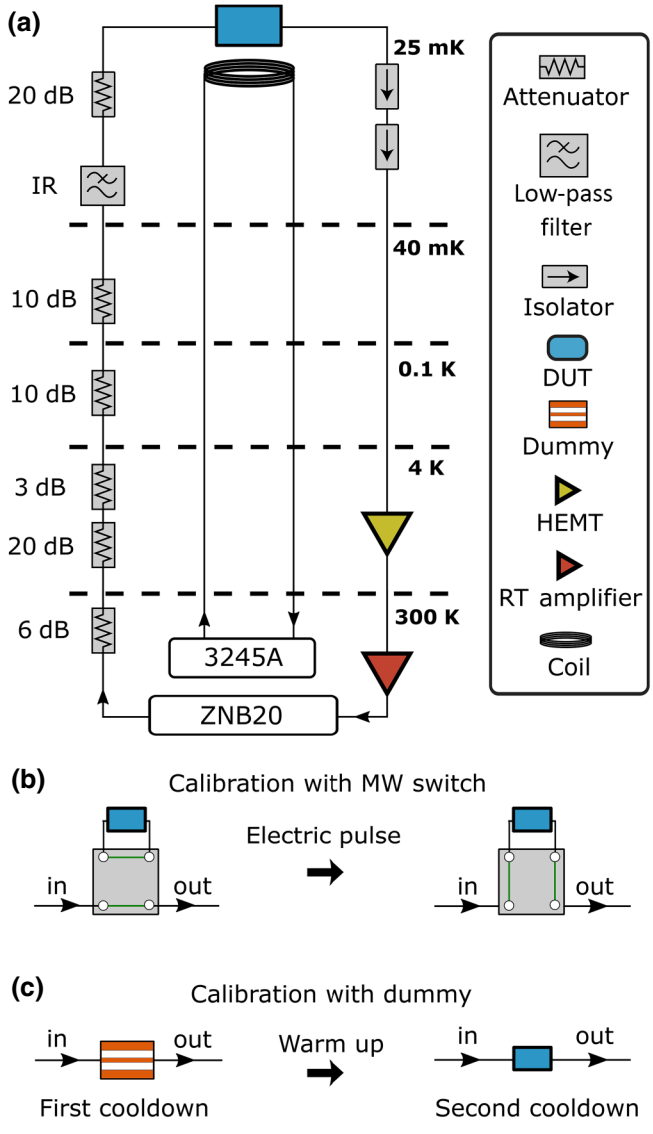


FIG. 10. Experimental setup and calibration technique. MW, microwave. RT, room temperature.


[1] G. Agrawal, *Nonlinear Fiber Optics*, Optics and Photonics (Elsevier, Burlington, MA, 2012), 5th ed.

[2] H. J. McGuinness, M. G. Raymer, C. J. McKinstrie, and S. Radic, Quantum Frequency Translation of Single-Photon States in a Photonic Crystal Fiber, Phys. Rev. Lett. **105**, 093604 (2010).

[3] D. M. Pozar, *Microwave Engineering* (John Wiley & Sons, Hoboken, 2009).

[4] R. J. Schoelkopf and S. M. Girvin, Wiring up quantum systems, Nature **451**, 664 (2008).

[5] M. H. Devoret, *Quantum Fluctuations in Electrical Circuits*, edited by S. Reynaud, S. Giacobino, and J. Zinn-Justin (Les Houches, 1995).

[6] C. C. Chin, D. E. Oates, G. Dresselhaus, and M. S. Dresselhaus, Nonlinear electrodynamics of superconducting NbN and Nb thin films at microwave frequencies, Phys. Rev. B **45**, 4788 (1992).

[7] A. Wallraff, D. I. Schuster, A. Blais, L. Frunzio, R.-S. Huang, J. Majer, S. Kumar, S. M. Girvin, and R. J. Schoelkopf, Strong coupling of a single photon to a superconducting qubit using circuit quantum electrodynamics, Nature **431**, 162 (2004).

[8] O. Astafiev, A. M. Zagoskin, A. A. Abdumalikov, Y. A. Pashkin, T. Yamamoto, K. Inomata, Y. Nakamura, and J. S. Tsai, Resonance fluorescence of a single artificial atom, Science **327**, 840 (2010).

[9] M. A. Castellanos-Beltran, K. D. Irwin, G. C. Hilton, L. R. Vale, and K. W. Lehnert, Amplification and squeezing of quantum noise with a tunable Josephson metamaterial, Nat. Phys. **4**, 928 (2008).

[10] C. Macklin, K. O'Brien, D. Hover, M. Schwartz, V. Bolkhovsky, X. Zhang, W. Oliver, and I. Siddiqi, A near–quantum-limited josephson traveling-wave parametric amplifier, Science **350**, 307 (2015).

[11] T. White, J. Mutus, I.-C. Hoi, R. Barends, B. Campbell, Y. Chen, Z. Chen, B. Chiaro, A. Dunsworth, E. Jeffrey, *et al.*, Traveling wave parametric amplifier with josephson junctions using minimal resonator phase matching, Appl. Phys. Lett. **106**, 242601 (2015).

[12] B. H. Eom, P. K. Day, H. G. Leduc, and J. Zmuidzinas, A wideband, low-noise superconducting amplifier with high dynamic range, Nat. Phys. **8**, 623 (2012).

[13] C. Bockstiegel, J. Gao, M. R. Vissers, M. Sandberg, S. Chaudhuri, A. Sanders, L. R. Vale, K. D. Irwin, and D. P. Pappas, Development of a broadband NbTiN traveling wave parametric amplifier for MKID Readout, J. Low Temp. Phys. **176**, 476 (2014).

[14] M. R. Vissers, R. P. Erickson, H. S. Ku, L. Vale, X. Wu, G. C. Hilton, and D. P. Pappas, Low-noise kinetic inductance traveling-wave amplifier using three-wave mixing, Appl. Phys. Lett. **108**, 012601 (2016).

[15] S. Chaudhuri, D. Li, K. D. Irwin, C. Bockstiegel, J. Hubmayr, J. N. Ullom, M. R. Vissers, and J. Gao, Broadband parametric amplifiers based on nonlinear kinetic inductance artificial transmission lines, Appl. Phys. Lett. **110**, 152601 (2017).

[16] Y. Krupko, V. D. Nguyen, T. Weissl, E. Dumur, J. Puertas, R. Dassonneville, C. Naud, F. W. J. Hekking, D. M. Basko, O. Buisson, N. Roch, and W. Hasch-Guichard, Kerr nonlinearity in a superconducting Josephson metamaterial, Phys. Rev. B **98**, 094516 (2018).

[17] L. Planat, R. Dassonneville, J. Puertas Martinez, F. Foroughi, O. Buisson, W. Hasch-Guichard, C. Naud, R. Vijay, K. Murch, and N. Roch, Understanding the Saturation Power of Josephson Parametric Amplifiers Made from SQUID Arrays, Phys. Rev. Appl. **11**, 034014 (2019).

[18] S. K. Tolpygo, V. Bolkhovsky, T. J. Weir, L. M. Johnson, M. A. Gouker, and W. D. Oliver, Fabrication process and properties of fully-planarized deep-submicron Nb/Al–$AlO_x$/Nb Josephson junctions for VLSI circuits, IEEE Trans. Appl. Supercond. **25**, 1 (2015).

[19] A. A. Adamyan, S. E. de Graaf, S. E. Kubatkin, and A. V. Danilov, Superconducting microwave parametric amplifier based on a quasi-fractal slow propagation line, J. Appl. Phys. **119**, 083901 (2016).

[20] P. Jung, S. Butz, S. V. Shitov, and A. V. Ustinov, Low-loss tunable metamaterials using superconducting circuits with Josephson junctions, Appl. Phys. Lett. **102**, 062601 (2013).

[21] C. Hutter, E. A. Tholen, K. Stannigel, J. Lidmar, and D. B. Haviland, Josephson junction transmission lines as tunable artificial crystals, Phys. Rev. B **83**, 014511 (2011).

[22] L. Planat, A photonic crystal josephson traveling wave parametric amplifier, arXiv:1907.10158 (2019).

[23] F. Lecocq, I. M. Pop, Z. Peng, I. Matei, T. Crozes, T. Fournier, C. Naud, W. Guichard, and O. Buisson, Junction fabrication by shadow evaporation without a suspended bridge, Nanotechnology **22**, 315302 (2011).

[24] J. Puertas Martinez, S. Leger, N. Gheeraert, R. Dassonneville, L. Planat, F. Foroughi, Y. Krupko, O. Buisson, C. Naud, W. Hasch-Guichard, S. Florens, I. Snyman, and N. Roch, A tunable Josephson platform to explore many-body quantum optics in circuit-QED, npj Quantum Inf. **5**, 1829 (2019).

[25] N. Masluk, I. Pop, A. Kamal, Z. Minev, and M. Devoret, Microwave Characterization of Josephson Junction Arrays: Implementing a Low Loss Superinductance, Phys. Rev. Lett. **109**, 137002 (2012).

[26] T. Weissl, B. Küng, E. Dumur, A. K. Feofanov, I. Matei, C. Naud, O. Buisson, F. W. J. Hekking, and W. Guichard, Kerr coefficients of plasma resonances in Josephson junction chains, Phys. Rev. B **92**, 104508 (2015).

[27] A. Fay, Ph.D. thesis, Université Joseph-Fourier – Grenoble I, (2008).

[28] K. Gupta, R. Garg, I. Bahl, and P. Bhartia, *Microstrip Lines and Slotlines*, Artech House Microwave Library (Artech House, Boston, 1979).

[29] M. V. Schneider, Microstrip lines formicrowave integrated circuits, Bell Syst. Techn. J. **48**, 1421 (1968).

[30] C. Deng, M. Otto, and A. Lupascu, Characterization of low-temperature microwave loss of thin aluminum oxide formed by plasma oxidation, Appl. Phys. Lett. **104**, 043506 (2014).

[31] J. Sambles, K. Elsom, and D. Jarvis, The resistivity of thin gold films, Solid State Commun. **32**, 997 (1979).

[32] By taking $\sigma = 2.5$ GS/m and $W = 50$ $\mu$m (the width where the current flows in the top ground) and considering the surface resistivity to be $R_{s,0} = \sqrt{\omega\mu_0/2\sigma}$, we obtain $L_c = \sqrt{2\pi\mu_0}/Z_c W\sqrt{2\sigma} = 1.5 \times 10^{-5}$ $\mathrm{m}^{-1}\,\mathrm{Hz}^{-1/2}$. This value, in the fits shown in Fig. 4, makes no difference with $L_c = 0$.

[33] We estimate the total setup attenuation to be $76 \pm 3$ dB as the sum of discrete attenuators (69 dB), cable attenuation (5 dB), and a filter (2 dB).

[34] A. B. Zorin, M. Khabipov, J. Dietel, and R. Dolata, in *2017 16th International Superconductive Electronics Conference (ISEC)* (2017), p. 1.

[35] A. B. Zorin, Josephson traveling-wave parametric amplifier with three-wave mixing, Phys. Rev. Appl. **6**, 034006 (2016).

[36] M. T. Bell and A. Samolov, Traveling-wave parametric amplifier based on a chain of coupled asymmetric squids, Phys. Rev. Appl. **4**, 024014 (2015).

[37] W. Zhang, W. Huang, M. E. Gershenson, and M. T. Bell, Josephson metamaterial with a widely tunable positive or negative kerr constant, Phys. Rev. Appl. **8**, 051001 (2017).

[38] A. L. Grimsmo and A. Blais, Squeezing and quantum state engineering with josephson travelling wave amplifiers, npj Quantum Inf. **3**, 20 (2017).

[39] E. Dumur, Ph.D. thesis, University Grenoble Alpes, (2015).